Precambrian Research 338 (2020) 105588

Contents lists available at ScienceDirect

Precambrian Research

journal homepage: www.elsevier.com/locate/precamres

Evolution of the Western Ethiopian Shield revealed through U-Pb geochronology, petrogenesis, and geochemistry of syn- and post-tectonic intrusive rocks

Shelby Bowden[a,b,*], Nahid D. Gani[a], Tadesse Alemu[c], Paul O'Sullivan[d], Bekele Abebe[e], Kibre Tadesse[f]

[a] *Department of Geography and Geology, Western Kentucky University, 1906 College Heights Blvd. #31066, Bowling Green, KY 42101, USA*
[b] *Department of Geosciences, Pennsylvania State University, 201 Old Main, University Park, PA 16802, USA*
[c] *Ethiopian Construction Design and Supervision Works Corporation, Addis Ababa, Ethiopia*
[d] *GeoSep Services LLC, 1521 Pine Cone Road, Moscow, ID 83843, USA*
[e] *Addis Ababa University, Addis Ababa, Ethiopia*
[f] *Dangote Cement (Ethiopia) PLC, Addis Ababa, Ethiopia*

ARTICLE INFO

Keywords:
East African Orogen
Western Ethiopian Shield
Mozambique Belt
Arabian-Nubian Shield
Geochronology
Geochemistry

ABSTRACT

Ethiopian basement formed between 850 and 450 Ma during the East African Orogen and represents the junction of the two distinct basement types found in Africa and Saudi Arabia: the low-grade Arabian-Nubian Shield and the high-grade Mozambique Belt. While many other localities along the East African Orogenic belt are well studied and despite the huge potential insight it could grant to the orogen's evolution, Ethiopian Basement is poorly understood. This study aims to understand the tectonic evolution of the East African Orogen in Ethiopia through the examination of the age, origin, and evolution of previously unmapped syn- and post-tectonic plutons intruded into the Western Ethiopian Shield's eastern edge. Dabana granite pluton crystallization ages were determined through U-Pb geochronological dating, and structural history was revealed through field mapping and thin section petrographic analysis. Whole rock elemental composition was determined through XRF (X-ray fluorescence) and ICP-OES (Inductively Coupled Plasma Optical Emission Spectrometry) methods to investigate petrogenesis and chemical evolution of the plutonic rocks. Results indicate this pluton formed during three intrusive periods under distinct tectonic domains that represent an evolving convergent margin. The oldest granite dates to 797.6 Ma and is associated with hydrous melting during volcanic arc subduction, followed by post-subduction related anhydrous magmatism at 774.6 Ma. The youngest granites date to 635–639 Ma and are evidence of late-stage crustal thickening in the final stage of collision. Two metamorphic episodes are recorded in the structure and petrography, which formed gneiss during high-grade metamorphism at 775.22 Ma and low-grade deformation around 630 Ma. This study presents the first geochronological and geochemical data from plutonic rocks in the study area, and grants valuable insight into the dynamics and evolution of the East African Orogen in Ethiopia.

1. Introduction

The positioning of East African Precambrian rocks between East and West Gondwana during the East African Orogen (EAO) makes this region paramount to unraveling the EAO's complex tectonic history (Fig. 1). Ethiopia resides at the junction of two distinct basements formed during the EAO: the low-grade, juvenile Arabian-Nubian Shield (ANS) to the north, and the high-grade metamorphic Mozambique Belt (MB) to the south (Figs. 1 and 2; Stern, 1994; Yibas et al., 2002; Abbate et al., 2015). While previous studies have begun to unravel Ethiopia's basement history (e.g. Ayalew and Johnson, 2002; Yihunie and Tesfaye, 2002; Allen and Tadesse, 2003; Yihunie, 2003; Stern et al., 2012; Blades et al., 2015, 2017), studies are still few due to limited basement access and exposure resulting from thick sedimentary and volcanic cover. Additionally, existing studies are spread over a vast geographic area covering the Southern Ethiopian Shield, Western Ethiopian Shield, and the northern Tigrai region.

This study investigates the age and petrogenesis of Dabana granite

* Corresponding author.
E-mail address: ShelbyMBowden@gmail.com (S. Bowden).

https://doi.org/10.1016/j.precamres.2019.105588
Received 19 October 2018; Received in revised form 22 December 2019; Accepted 22 December 2019
Available online 24 December 2019
0301-9268/ © 2019 Elsevier B.V. All rights reserved.

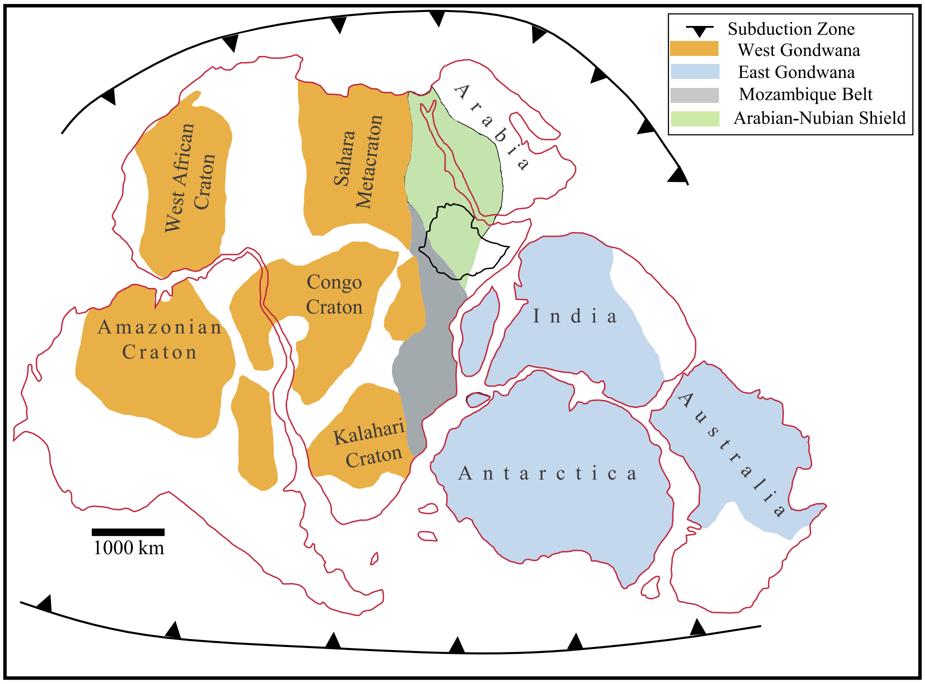

Fig. 1. . Reconstruction of the East African Orogen, highlighting the relative collision of the East and West Gondwana with Ethiopia situated at the junction of the Arabian-Nubian Shield (ANS) and the Mozambique Belt (modified from Tsige and Abdelsalam, 2005; Abdelsalam et al., 2008; Meert and Lieberman, 2008; Goodenough et al., 2010; Abdelsalam et al., 2011; Stern et al., 2012).

intrusive rocks in the Western Ethiopian Shield's (WES) eastern edge (Fig. 2). Methods used include zircon U-Pb geochronological dating, major and trace element geochemical analysis, thin section petrography, and structural analysis. Other studies in the area that have employed similar methods include Kebede et al. (1999, 2001a, 2001b, 2007), Woldemichale et al. (2010), and Blades et al. (2015, 2017). These aforementioned studies largely focused on the larger intrusions in the WES and the relationships between these regional plutonic bodies. In contrast, we examined a small intrusion in high resolution and great detail, which highlights the tectonic and geochemical complexity of even the very small intrusions in the WES. These data provide a robust understanding of how and when these rocks formed, as well as their evolution since formation.

2. Geological Setting

2.1. Tectonic history

The EAO is widely considered as an example of a Neoproterozoic-Cambrian Wilson Cycle ocean basin evolution (Stern, 1994; Worku and Schandelmeier, 1996; Fritz et al., 2013). Zircon U-Pb dating places ANS formation in the Neoproterozoic-Early Cambrian during Mozambique Ocean closure, although around 5% of zircons in ANS rocks have much older ages, attributed to either mantle or detrital zircon sourcing by Sr, Nd, Hf, and Pb isotopic ratios (Stern and Kroner, 1993; Stern, 1994; Divi et al., 2001; Stern, 2002; Stern et al., 2010; Johnson et al., 2011; Fritz et al., 2013). From 750 to 650 Ma, the ANS collided with East and West Gondwana in an escape tectonics, Tibetan-type collision, remobilizing older MB-related crust and causing igneous intrusions throughout the Neoproterozoic-Early Cambrian (Bonavia and Chorowicz, 1992; Muhongo and Lenior, 1994; Stern, 1994; Abdelsalam and Stern, 1996; Chen, 2001; Muhongo et al., 2001; Yibas et al., 2002; Yihunie, 2003). The EAO-related crust is exposed in Ethiopia as a series of restricted basement shields (Kebede et al., 1999; Johnson et al., 2004; Abdelsalam et al., 2008; Stern et al., 2012; Blades et al., 2015, 2017). Two of the largest shields are located in southern and western Ethiopia, termed the Southern Ethiopian Shield (SES) and Western Ethiopian Shield (WES), respectively (Fig. 2; Ayalew and Johnson, 2002; Stern et al., 2012). Both shields are characterized by accreted volcanic arc, high-grade gneissic, and magmatic intrusion terranes (Kebede et al., 1999; Johnson et al., 2004; Abdelsalam et al., 2008; Stern et al., 2012; Blades et al., 2015, 2017).

The ANS is composed of isotopically juvenile crust characterized by greenschist-grade metamorphosed island arc, back-arc, and ophiolite-decorated sutures (Stern, 1994; Abdelsalam and Stern, 1996; Teklay et al., 1998; Ayalew and Johnson, 2002; Tsige, 2006; Avigad et al., 2007). The majority of ANS crust outcrops in Saudi Arabia, Sudan, and Egypt, although ANS exposures extend as far south as Kenya while transitioning to progressively older MB crust (Abdelsalam and Stern, 1996; Stern, 2002). Other than rock type, age and location, isotopic ratios have proved very useful in distinguishing the juvenile, mantle-related ANS melts from the more varied, remobilized crustal signatures characteristic of MB rocks (e.g. Moller et al., 1998; Stern, 2002; Stern et al., 2010; Blades et al., 2015). In contrast to the ANS, MB rocks are characterized by higher-grade gneissic metamorphism over a longer tectonic history extending to pre-Neoproterozoic orogenic cycles (Stern, 1994; De Waele et al., 2006; Bingen et al., 2009; Fritz et al., 2013). MB rocks dominate the southern EAO, and presence in Ethiopia is debated based on crustal isotopic signatures in some rocks from the WES, high-grade gneissic rocks sandwiching juvenile crust, and spatial locations along island-arc suture zones (Ayalew et al., 1990; Ayalew and Peccerillo, 1998; Allen and Tadesse, 2003; Blades et al., 2015). Although there is support in the literature for the presence of MB rocks in the Ethiopian shields (e.g. Ayalew et al., 1990; Ayalew and Peccerillo, 1998; Allen and Tadesse, 2003; Avigad et al., 2007), the evidence is restricted to very few isotopic studies and rock type associations.

2.2. Western Ethiopian Shield (WES)

The WES consists of high-grade metamorphic rocks, *meta*-volcanic rocks, *meta*-sedimentary rocks, and both mafic and felsic intrusions (Fig. 3A; Alemu and Abebe, 2000; Ayalew and Johnson, 2002; Allen and Tadesse, 2003; Alemu and Abebe, 2007; Woldemichale et al., 2010; Blades et al., 2015, 2017). These lithologic units are found in several accreted arc terranes that formed from subduction, intrusion, and metamorphism during collision and crustal thickening (Ayalew and Johnson, 2002; Woldemichale et al., 2010; Blades et al., 2015, 2017). The WES has been classified in several ways, but this study employs the

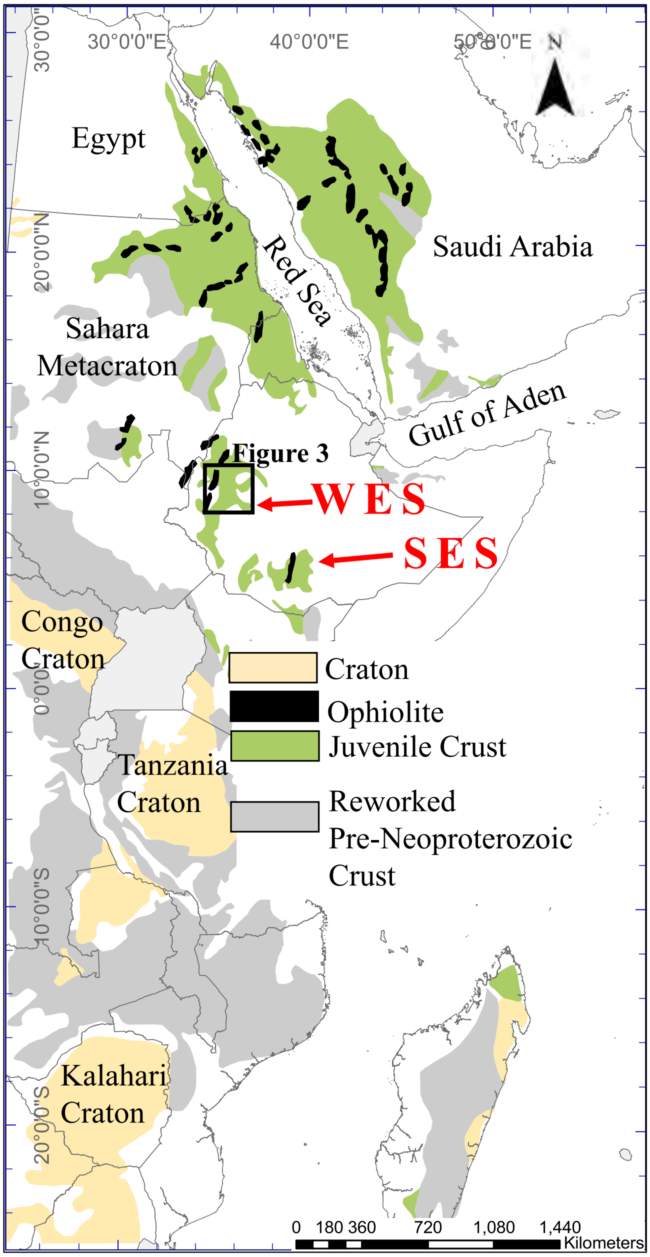

Fig. 2. . Current setting of major rock units along the EAO, highlighting pre-Neoproterozoic rocks (including the MB), cratons, and juvenile crust, which includes the Arabian-Nubian Shield. Ethiopian basement rocks are exposed in a number of shields, shown here as the Western Ethiopian Shield (WES) and Southern Ethiopian Shield (SES). The box shows the location of Fig. 3 (adapted from Stern, 1994; Abdelsalam and Stern, 1996; Worku, 1996; Stern, 2002; Tsige and Abdelsalam, 2005; Fritz et al., 2013).

criteria set forth by Allen and Tadesse (2003), which describes the WES by five lithologically-distinct domains: (from east to west) the Didessa, Kemashi, Dengi, Sirkole, and Daka domains. The outer Didessa and Daka domains are largely high-grade para and orthogneiss, intruded in some areas by Neoproterozoic intrusions. These domains have been interpreted to represent a northern segment of the MB by several authors, based mainly on rock type similarities with the southern portions of the MB, but isotopic studies are needed to confirm this interpretation (Ayalew and Johnson, 2002; Yibas et al., 2002; Allen and Tadesse, 2003). The inner domains are lower grade and could be a southern extension of the ANS (Ayalew and Johnson, 2002).

2.3. Structures

Accretion and deformation that formed the WES lasted from around 800–620 Ma during the main collision of the EAO (Alemu and Abebe, 2007). Three deformational events, D1, D2, and D3, have been recognized within the WES and are useful for classifying rocks from the Dabana Pluton (Ayalew and Johnson, 2002; Allen and Tadesse, 2003; Johnson et al., 2004; Alemu and Abebe, 2007; Yihunie and Hailu, 2007). The earlier D1 event is characterized by large, isoclinal, recumbent folds that have NNE-SSW striking axial planes and are termed F1 (Alemu and Abebe, 2007; Yihunie and Hailu, 2007). The plunge is between 5°–10° NE and SW. During D1 deformation, NNE-SSW striking and westward dipping foliation (S1) developed within terranes around the study area, which is often parallel to the fold axial planes (Ayalew and Johnson, 2002; Johnson et al., 2004; Alemu and Abebe, 2007). The later D2 event formed N-S striking upright folds (F2) superimposed on D1 folding during east–west shortening (Ayalew and Johnson, 2002; Alemu and Abebe, 2007). D2 foliation (S2) occurs in schistosic and crenulation structures planar to D2 folds, often making S2 determinations difficult (Alemu and Abebe, 2007). Late transpressive brittle-shearing and folding are associated with the youngest D3 event, which formed mylonite, augens, steeply-plunging folds (F3), and shear bands in WES rocks (Ayalew and Johnson, 2002; Johnson et al., 2004; Alemu and Abebe, 2007). D3 resulted in N, NNE, and NW trending strike-slip faults, shear zones, and both primary sinistral and secondary dextral movement (Alemu and Abebe, 2007).

The rocks are also classified based on their metamorphism since all (except for the very late intrusions) are metamorphosed. M1 is a high-temperature gneissic to upper amphibolite facies event that occurred before D2, and is associated with peak conditions of 600-800 °C and 5–8 kbar (Ayalew and Johnson, 2002). M2 is a low-temperature amphibolite facies that may also have involved aqueous fluids as evidenced from epidote and hornblende replacement products (Ayalew and Johnson, 2002). M2 likely resulted from late crustal thickening during D3 (Ayalew and Johnson, 2002; Johnson et al., 2004).

3. Methods

3.1. U-Pb geochronology

Rock samples were crushed, washed, and sieved with 355 μm mesh. Zircons were separated from crushed samples using standard magnetic and heavy liquid (methylene iodide and lithium metatungstate) separation techniques before mounting in epoxy wafers and manually abrading to reduce surface-related Pb loss. Wafers containing zircons were washed in 5.5 M HNO_3 for 20 s at 21 °C before laser analysis.

Laser ablation inductively-coupled plasma-mass spectrometry (LA-ICP-MS) analysis was conducted at the Washington State University's Geoanalytical Laboratory using a ThermoScientific Element2 mass spectrometer connected to a New Wave 213 nm laser ablation system. Each sample underwent 25–30 analyses with a 20 μm spot size at 5 Hz, and each spot was analyzed with 200 scans. Wide varieties of spot locations were selected from both magmatic and metamorphic zircons, rims and cores, and different zonation types to collect age data from the full range of geologic events through which the zircons were subjected.

Standards used included the Duluth complex FC and F5, Fish Canyon Tuff IF, Mount Dromedary MD, Temora 2 Middledale gabbroic diorite T2, and Tardree Rhyolite TR, which encompasses a wide standard age range from 1099 to 61.23 Ma. Data were reduced using the IsoplotR program developed by Pieter Vermeesch (Vermeesch, 2018), and common Pb was subtracted using the Stacey and Kramer (1975) model. Zircon characteristics such as zonation, shape, size, and inclusions were observed using a backscatter electron detector attached to a scanning electron microscope (SEM-BSE) at Western Kentucky University's Electron Microscopy lab.

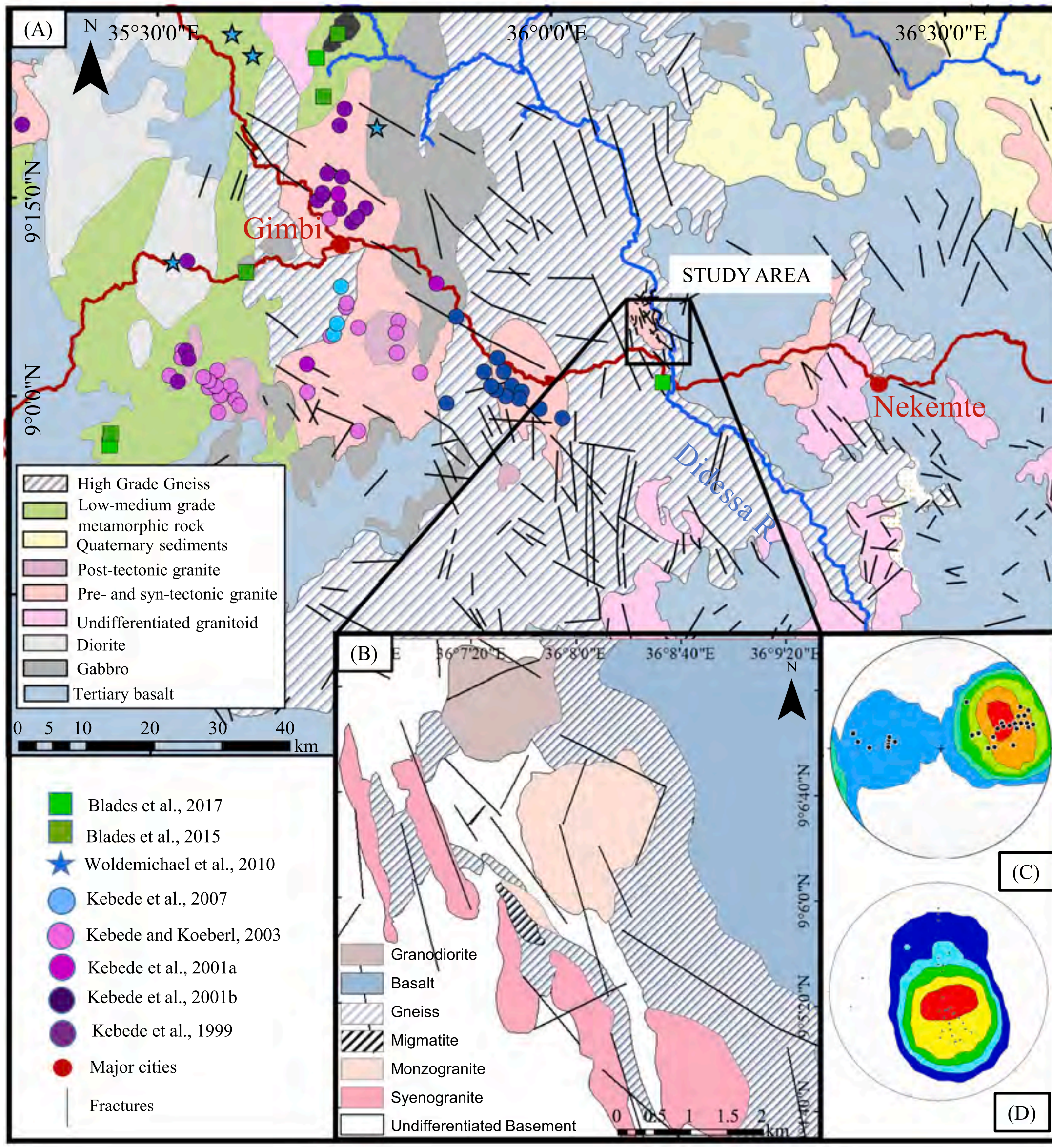

Fig. 3. . (A) The geology and structure of the region surrounding the study area, highlighting the relative lack of nearby studies and location within a primarily gneissic terrane. Published geochronological and geochemical studies in the surrounding areas shown by symbols described in the legend. (B) Detailed study area geological map created from field data, SRTM DEM, and geological quadrangle maps (modified from Tefera and Berhe, 1987; Kebede et al., 1999, 2001a, 2001b, 2007; Gerra and Hailemariam, 2000; Kebede and Koeberl, 2003; Woldemichale et al., 2010; Alemu, 2014; Blades et al., 2015, 2017) (C) Contoured plane to poles of faults within the study area (black box in Fig. 3A). The dominant strike is NNW with secondary NNE trends. Dip ranges from 30 to 70°, with an average dip of 50°. (D) Contoured plane to poles of foliation and lineaments measured in the field (black box in Fig. 3A). Foliation is nearly always north-trending with steep plunges to the west.

3.2. Whole rock geochemistry

Samples were cleaned of weathered surfaces and powdered with an agate mortar and pestle. Elemental data was collected through inductively-coupled plasma-optical emission spectrometry (ICP-OES; Table 1). Samples were dissolved in hydrofluoric acid and aqua regia and prepared according to the American Society for Testing and Materials (ASTM) D6357-11 method using standard SRM 2711a.

In addition to ICP-OES, sample results were independently verified through X-ray fluorescence (XRF) analysis. Glass disks for wavelength dispersive X-ray fluorescence spectrometer (WDXRF) analysis were prepared at the Kentucky Geological Survey office by mixing 4.0 g of sample with 8.0 g of GF-9010 flux (90% lithium tetraborate and 10% lithium fluoride) and fusing the disks in a Katanax K1Prime auto fluxer. Disks were analyzed in a Bruker AXS S4 Pioneer WDXRF for elemental composition. Standards run alongside the samples were GSP-1, YG1, GRI-1, and KPT-1, which were used in conjunction with 24 other standards to create calibration factors used in data reduction.

4. Results

4.1. Petrographic and structural analysis

4.1.1. Granodiorite (G1-5)

Rock types were determined from modal percentages gleaned from thin section mapping (QAP plot not shown). Following structural observations, the rocks' deformation, folding, and foliation histories were categorized according to the criteria used by Alemu and Abebe (2000), Ayalew and Johnson (2002), and Johnson et al. (2004) described above (e.g. D1, F1, etc.). Granodiorite outcrops are found at the base of the

Table 1
Whole rock geochemical results reduced from ICP-OES analysis. Major oxides are represented as weight percent, while trace elements are presented in parts per million (ppm).

	Granodiorite					Monzogranite										Syenogranite		Migmatite		
						N-S Folded								NE-SW Folded						
Sample	G1	G2	G3	G4	G5	G6	G7	G8	G9	G10	G11	G12	G13	G14	G15	G16	G17	G18	G19	G20
(wt%)																				
SiO_2	68.34	65.14	66.86	69.23	68.89	70.73	71.08	71.15	74.46	69.53	69.89	75.03	72.28	69.96	72.67	74.37	69.35	69.98	67.55	62.64
TiO_2	0.37	0.52	0.43	0.21	0.27	0.15	0.21	0.02	0.07	0.22	0.23	0.04	0.22	0.15	0.16	0.20	0.22	0.55	0.63	0.75
Al_2O_3	17.54	17.94	17.83	17.06	17.31	15.49	15.32	15.72	14.25	15.54	16.31	12.25	12.54	14.19	13.92	13.24	13.57	15.41	14.49	18.08
Fe Total	3.28	3.93	3.52	2.45	2.75	0.98	1.46	0.42	0.37	1.78	1.84	0.75	1.78	2.16	1.62	1.24	2.34	4.02	3.94	6.61
MnO	0.04	0.00	0.06	0.02	0.03	0.00	0.02	0.00	0.00	0.02	0.03	0.01	0.02	0.04	0.02	0.01	0.04	0.06	0.08	0.16
MgO	1.13	1.56	1.27	0.56	0.73	0.14	0.24	0.12	0.08	0.42	0.43	0.04	0.08	0.34	0.12	0.08	0.21	1.37	1.29	1.89
CaO	3.60	3.82	3.71	2.89	3.18	0.93	1.10	1.14	0.82	1.45	1.54	1.00	0.89	0.52	0.29	0.46	0.37	2.20	4.46	5.30
Na_2O	4.19	4.59	4.15	3.51	3.71	2.97	2.15	2.74	1.95	3.34	3.13	3.84	3.94	3.11	3.83	3.54	4.46	3.62	4.61	3.57
K_2O	1.68	1.49	1.87	2.49	2.16	6.11	6.21	5.80	6.18	4.95	4.70	4.89	6.21	6.25	6.01	5.05	6.70	1.88	1.36	1.14
P_2O_6	0.20	0.38	0.32	0.15	0.18	0.05	0.08	0.02	0.04	0.09	0.11	0.02	0.12	0.29	0.04	0.02	0.34	0.07	0.08	0.15
LOI	0.00	0.91	0.23	0.86	0.50	0.76	0.84	1.08	0.89	0.90	1.39	1.07	1.26	1.59	0.89	0.48	1.46	0.71	1.14	0.25
Total	100.37	100.28	100.25	99.43	99.71	98.31	98.71	98.21	99.11	98.24	99.60	98.94	99.34	98.60	99.57	98.69	99.06	99.87	99.63	100.54
(ppm)																				
V	58.00	62.00	63.00	45.00	57.00	12.00	10.00	4.00	5.00	20.00	20.00	4.21	20.00	4.76	4.52	3.90	5.12	40.00	41.00	39.00
Cr	11.78	9.64	5.67	< 5	7.73	7.25	6.37	< 5	< 5	7.75	8.44	16.69	7.76	< 5	< 5	< 5	5.27	12.90	12.42	11.57
Co	5.89	8.60	7.92	5.83	7.14	3.94	4.23	5.03	5.11	4.75	3.65	< 2	< 2	2.33	3.16	4.21	5.71	6.60	6.73	8.21
Ni	6.18	7.69	3.24	4.93	5.51	7.77	7.53	8.04	8.37	7.10	7.12	8.74	7.11	6.76	7.28	7.37	8.16	5.87	6.73	8.21
Cu	26.85	25.47	28.26	21.64	25.56	23.26	24.94	27.44	26.75	25.65	25.06	21.48	25.65	18.49	21.48	20.28	22.47	22.07	22.07	21.00
Zn	60.00	62.00	54.00	87.00	65.00	34.00	42.00	30.00	29.00	46.00	47.00	32.00	46.00	39.00	50.00	314.00	42.00	76.00	74.00	64.00
Ga	11.00	16.00	15.00	13.00	13.00	10.00	10.00	9.00	11.00	12.00	11.00	13.00	31.00	11.00	48.00	43.00	22.00	12.00	13.00	12.00
Rb	62.29	43.21	51.16	65.23	63.72	127.20	126.24	123.14	124.16	141.97	152.23	70.62	51.97	78.28	124.38	99.27	112.17	63.74	67.48	72.18
Sr	750.34	1210.37	927.45	535.19	830.84	455.86	430.17	352.97	310.91	289.88	174.28	174.84	53.16	49.62	116.14	112.81	72.14	207.95	221.72	324.16
Y	< 5	< 5	< 5	< 5	< 5	< 5	< 5	< 5	< 5	< 5	< 5	77.75	71.38	67.25	84.52	89.52	78.16	58.88	22.59	17.74
Zr	145.76	112.50	128.39	168.39	147.25	194.67	176.34	161.36	110.37	225.34	212.54	113.25	225.23	233.87	213.19	163.97	258.34	254.83	279.04	131.49
Nb	6.24	5.63	6.87	7.11	6.46	7.45	8.24	< 5	7.16	5.51	5.64	7.61	24.60	14.19	16.38	13.97	18.27	17.01	16.65	15.27
Ba	375.00	453.00	428.00	279.00	313.00	1325.00	1537.00	2397.00	2178.00	1012.00	1089.00	1165.00	428.37	764.00	986.00	1140.00	852.34	882.00	916.00	602.87
La	71.00	54.00	68.00	75.00	67.00	76.00	87.00	71.00	68.00	90.00	88.00	64.00	102.00	113.00	72.00	68.00	84.00	87.00	90.00	75.00
Ce	13.00	16.00	14.00	22.00	16.00	66.00	49.00	42.00	71.00	44.00	58.00	8.00	44.00	78.00	108.00	11.00	64.00	67.00	77.00	74.00
Eu	0.28	0.36	0.35	0.22	0.30	0.29	0.21	0.07	0.05	0.29	2.89	0.22	0.30	1.79	0.72	0.04	1.24	1.52	1.64	1.24
Pb	24.81	32.50	30.25	27.60	28.79	30.72	28.42	29.53	30.49	31.72	29.53	33.08	30.72	23.63	30.72	31.90	26.17	29.53	27.18	25.38
Th	7.09	5.28	6.32	8.49	6.79	21.78	24.15	20.70	21.47	23.08	22.36	7.74	23.08	11.27	14.01	10.62	12.54	17.89	16.02	15.46
U	< 3	< 3	< 3	< 3	< 3	< 3	3.05	3.04	< 3	< 3	3.00	3.45	< 3	< 3	3.21	3.00	3.47	3.28	4.47	4.12

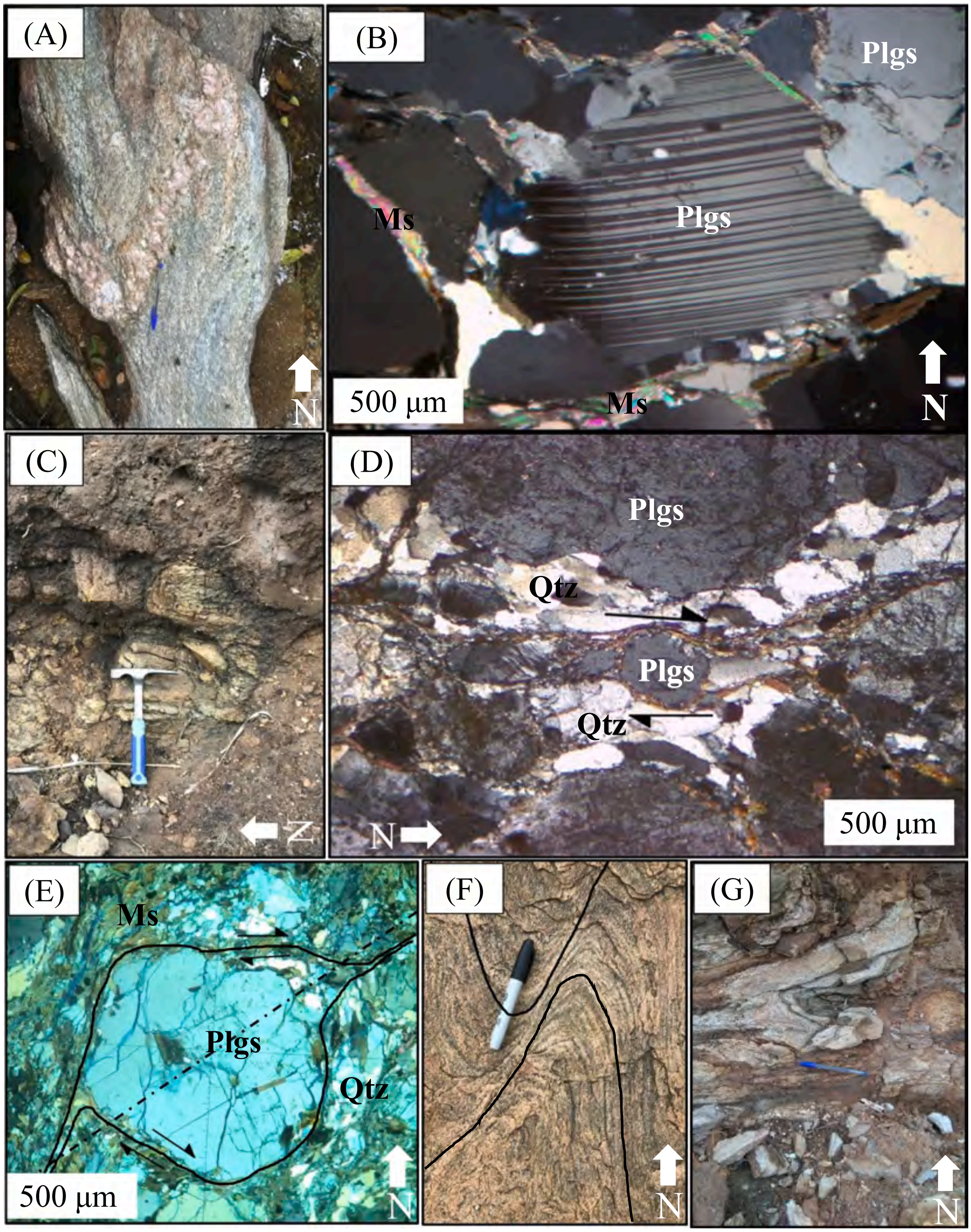

Fig. 4. . (A) Folded pegmatite vein from an adakite outcrop. Fold axial plane strikes N-S from E-W directed compression. (B) Deformed wedge-shaped albite lamellae from a granodiorite. (C) Folded outcrop of a monzogranite showing tight folds that have a N-striking axial plane. (D) δ-type porphyroclast from a monzogranite showing dextral shearing. (E) δ-type porphyroclast from a monzogranite thin section showing dextral shearing. (F) A syenogranite outcrop, showing north-striking folds that have undergone dextral transpression. (G) Migmatite outcrop showing NW-EW striking, isoclinal, recumbent folds (F1).

Didessa River in the northern part of the study area (Fig. 3). Due to seasonal flooding and flood bank deposits, exposure is limited around the Didessa River, and outcrops are most prevalent in tributaries that have uncovered the underlying bedrock. The outcrops form small cliffs that are in alignment with the regional structural trends, indicating that the outcrops are often exposed due to normal faulting (Fig. 3C).

The granodiorites exhibit a west-dipping gneissic mineral alignment that is sub-parallel to the dominant NNW structural trends, interpreted as S1 foliation resulting from M1 metamorphism (Fig. 3D). Outcrop-scale folds are tightly folded with an interlimb angle of ~ 40° (Fig. 4A). Recumbent, isoclinal folds are the most common and strike NE-SW (F1), followed by a secondary larger scale (meters to 10 s of meters) asymmetrical folds that strike N-S (F2), and finally a minor amount of shear movement (F3).

The granodiorites are uniformly coarse-grained with feldspar grain diameters ranging from < 1 to 4 mm, and consist mainly of plagioclase, alkali feldspar, and quartz. Albite overgrowth occurs on both the alkali feldspars and plagioclase, and lamellae are often deformed and wedge-shaped (Fig. 4B). Both feldspars have alterations of sericite, and the alkali feldspars are often microcline. Quartz is undulatory and interstitial. Micas are preferentially oriented and include both biotite and a minor amount of secondary white muscovite. Biotite is commonly altered to chlorite. Hornblende is common and often found within larger crystals such as the feldspars. Accessory minerals include abundant magnetite, apatite, and zircon.

4.1.2. N-S Folded monzogranite (G6-13)

These monzogranites are primarily exposed to the northeast of the study area and show variably weak foliation with a dominant trend that strikes N and dips around 40° to the west (likely F2; Fig. 3D). Folds are tight (interlimb angle ~ 30°), asymmetrical, and have N-striking axial planes (F2; Fig. 4C). The average grain size is slightly smaller than the granodiorites, but feldspars are still quite large and range from 1 to 4 mm in diameter. These monzogranites are mainly composed of alkali feldspars, plagioclase, and undulatory quartz, but have a greater abundance of quartz and micas than the granodiorites. The alkali feldspars are commonly microcline, have rare alterations to sericite, and perthite and biotite intergrowths. Plagioclase exhibits deformed albite lamellae. Interstitial muscovite and biotite are present, and both micas have a distinct preferential orientation parallel to the gneissosity. Cordierite is present but in minor amounts. Apatite, ilmenite, garnet, and zircon are common accessory minerals. Some δ and φ-type porphyroclasts are identifiable in thin section, indicating F3 dextral post-crystallization movement during D3 (Fig. 4D).

4.1.3. NE-SW folded monzogranite (G14 & 15)

Areas to the southwest of the monzogranite exposures have primarily isoclinal, recumbent, tight folds that strike NE-SW (F1) and are overprinted by N-S striking folds (F2) such as those observed in rocks G1-5. These monzogranites are adjacent to the migmatite, and define a folded but clear contact between the two rock types. Grain size is smaller than the other monzogranites, consisting primarily of feldspar megacrysts within a fine-grained quartz/mica/feldspar matrix. Feldspars are often microcline, have quartz and perthite intergrowths, and deformed and wedge-shaped lamellae. Both biotite and very minor muscovite are present and occur along with undulatory quartz in preferentially-oriented bands within interstitial spaces. Ilmenite, magnetite, and interstitial amphibole are found in minor amounts. Apatites are present but much smaller than in other rock suites. Feldspar porphyroclasts are present in both δ and φ-type (Fig. 4E).

4.1.4. Syenogranite (G16 & 17)

The syenogranites have clear gneissosity that strikes N, dips west, and is both folded and dextrally sheared. The intense folding has made a distinction between folding events difficult, but at least three distinct folding events are observable. The most prominent folds are N-striking (F2) isoclinal folds that have undergone secondary dextral shear (F3; Fig. 4F). A third, NE-SW striking fold series (F1) seems present but difficult to distinguish.

Grain size is nearly identical to the NE-SW folded monzogranite with similar mineral composition and characteristics. Undulatory quartz and micas compose the matrix and are preferentially oriented in alignment with gneissosity trends observed at the outcrop scale. Micas present are both biotite and muscovite and are interstitial. Minor amounts of magnetite, interstitial amphibole, and apatite are present.

4.1.5. Migmatite (G18–20)

The migmatites outcrop in a small area stratigraphically above the granodiorites and monzogranites (Fig. 3B). Although the adjoining NE-SW folded monzogranite to the northwest of the migmatites defines a folded contact (interlimb angle ~15–30°), the contact between the granites and migmatite is clear and shows limited mixing of the two lithologies at the outcrop scale. Gneissosity strikes north and dips to the west, and augens are visible in the outcrop. Folding is most similar to the NE-SW folded monzogranite, with primary NE-SW striking, isoclinal, recumbent folds that are overprinted by N-S striking folds and dextral shear (Fig. 4G).

The migmatites are composed mainly of feldspar megacrysts surrounded by undulatory quartz and micas. The feldspars are commonly microcline with sericite alteration, and plagioclase often has deformed and wedge-shaped lamellae. Together with muscovite, biotite is interstitial and oriented parallel to the outcrop-scale gneissosity. Augens are observed at all levels and form porphyroclasts that indicate dextral movement. Major differences in the paleosome and neosome are restricted to a grain size reduction and lack of biotite in the neosome. Hornblende and cordierite are present in the paleosome, with the former being more abundant and found within feldspars. The accessory minerals zircon, apatite, magnetite, and ilmenite are present in much greater abundance in the paleosome.

4.2. U-Pb dating

4.2.1. G1 (Granodiorite)

G1 zircons are generally uniform and range in length from 75 to 400 μm, with most of the zircons being around 200 μm long. Aspect ratios are consistently 2:1, and their shape is generally euhedral and prismatic pyramidal. Grains are pink to clear, translucent, and have few inclusions. Zircons have primarily concentric oscillatory zoning, well-defined cores, and recrystallization structures on the rims. A smaller population shows weak or no zoning with abundant recrystallization features.

All 25 analyzed zircon grains yielded concordant ages that range from 823 to 649 Ma and a combined concordia age of 752.70 ± 3.6 Ma (Mean Square Weighted Deviation, MSWD = 4.6). Th/U ratios are generally high (0.19–0.94) which suggests magmatic growth, with only two at or below 0.1. The seven youngest analyses show significant variance from the mean, six of which (including the two spots with low Th/U) show no zoning, five of which were taken on outer rims, and all of which define a spread on the $^{206}Pb/^{238}U$ plot which suggests Pb loss. Due to zoning characteristics and spot locations, these data are interpreted to result from a combination of Pb loss and metamorphism. Excluding these data and analysis 261AZ1_23, which also suggests Pb loss, D1 has a concordia age of 797.60 ± 4.80 Ma (MSWD = 0.14) (Fig. 5A) and a $^{206}Pb/^{238}U$ age of 796.50 ± 5.4 (MSWD = 0.4) (Fig. 5B). Given the lower MSWD, the concordia age of 797.60 ± 4.80 Ma is interpreted to represent the most likely magmatic crystallization age.

4.2.2. G6 (Monzogranite)

G6 contains zircons that are pink to clear in color. Length ranges from 75 to 400 μm, and aspect ratios vary from 2:1 up to 6:1 in very elongated grains. Two distinct zircon groups can be identified: Group 1 generally has a 2:1 or 3:1 aspect ratio, is subhedral to subrounded, translucent, and has few inclusions, while Group 2 has aspect ratios from 4:1 to 6:1, are elongated, prismatic pyramidal, opaque, and have frequent inclusions. Group 1 zircons have generally weak concentric oscillatory zoning with recrystallization features on the outermost rims; however, Group 2 zircons have a wide variety of zoning characteristics. Some zircons have oscillatory cores surrounded by a recrystallization zone, subsequent oscillatory zone, and a final homogenous outer rim, indicating multiple periods of growth. Other Group 2 zircons have a patchy or planar texture with at least one overgrowth rim. These characteristics suggest that the cores from Group 2 zircons represent inherited zircons that were altered from subsequent magmatic activity and metamorphism.

Analyses of 29 grains yielded concordant ages from 826 to 590 Ma. At least two generations of zircons are identifiable from the $^{206}Pb/^{238}U$ age plots, with a possible third within the older plateau. All the concordant scans yield a concordia age of 704.30 ± 2.70 Ma (MSWD = 0.31) (Fig. 5C), but when split into the separate plateaus, the concordia ages are 639.90 ± 5.1 Ma (MSWD = 0.4), 731.70 ± 5.50 (MSWD = 0.88), and 792.10 ± 5.0 (MSWD = 0.17). The oldest plateau age is within the range of the G1 rocks and may indicate a relationship as inherited zircons from a mixing contact not visible in the field (Fig. 5D). The middle plateau does not directly relate to other ages within the pluton, but could represent an additional generation of

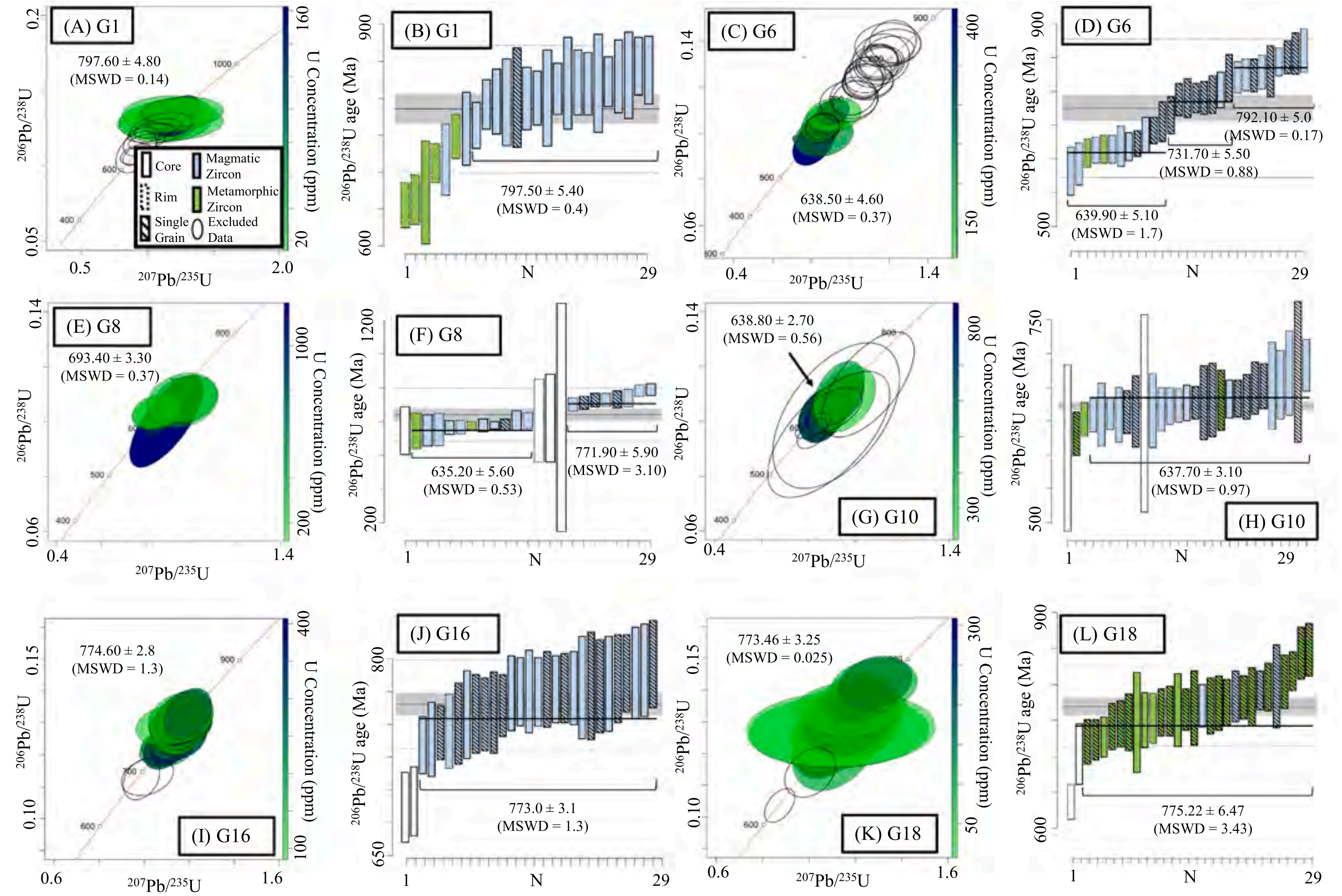

Fig. 5. . (A–L): Concordia plots and associated $^{206}Pb/^{238}U$ age plots, showing excluded analyses, spot locations, and type of spot. Common lead was corrected using the Stacey and Kramer calculation (1975). Error ellipses are 2-sigma.

inherited zircons and/or Pb loss. Most of the Th/U ratios were > 0.1, giving good reason to believe that most of the younger ages are due to magmatic growth and actual crystallization age of the G2 rocks, rather than metamorphic recrystallization; however, two grains have spots within a recrystallization dissolution texture and are considered unreliable due to their possible relationship with metamorphism. Excluding the metamorphic zircons, the $^{206}Pb/^{238}U$ age of the younger plateau is 639.90 ± 5.10 Ma (MSWD = 1.7) and the concordia age is 638.50 ± 4.6 Ma (MSWD = 0.37). We consider the concordia age (with lower MSWD) as the crystallization age of G2 (Fig. 5C).

4.2.3. G8 (Monzogranite)

G8 zircons are generally smaller than G1 and G6, with lengths varying from 75 to 220 µm. The aspect ratio is mainly 4:1, with some very elongated grains approaching 6:1. Grains are prismatic pyramidal, elongated, pale yellow to clear in color, opaque, and have frequent inclusions. Zircons from G8 exhibit characteristics (such as metamorphic overgrowth, low Th/U, recrystallization rims, and distinct plateau age populations) of inherited zircons and multiple periods of growth. Zoning is generally concentric and oscillatory, with some cloudy zoning within cores.

Scans from 30 grains yielded 23 spots with concordant scans, three of which have very high 2σ (> 100) and two of which have < 10 concordant scans, rending these five scans unreliable. Several analyses have a Th/U ratio of < 0.1, most of which are younger grains that exhibit variance parallel to the abscissa, suggesting metamorphic growth around 630 Ma that is synchronous with magmatic growth. However, four of the scans with low Th/U are clearly in a magmatic growth zone due to the presence of concentric oscillatory zoning. These relationships highlight the limitations of using Th/U as a standalone indicator of metamorphic growth.

All concordant scans yield an age of 693.40 ± 3.30 Ma (MSWD = 7.2), but two distinct plateaus are observed on the $^{206}Pb/^{238}U$ age plot, suggesting two distinct zircon generations (Fig. 5E and F). Because analysis spots that are within magmatic zonation define both the younger and older plateaus, we consider the older plateau to represent the ages of inherited zircons (771.90 ± 5.90 Ma, or roughly the same age as G1), while the younger plateau represents the most recent magmatic crystallization age. Some of the analyses have a high error that we attribute to Pb loss and metamorphism and are not included in the concordia age. Selecting the concordant scans from the younger plateau that do not seem affected by metamorphism, those with > 10 concordant scans, and without Pb loss, the G8 rocks have a concordia age of 638.10 ± 5.10 Ma (MSWD = 1.7) and a $^{206}Pb/^{238}U$ age of 635.20 ± 5.60 Ma (MSWD = 0.53). The variance between the concordia age and the $^{206}Pb/^{238}U$ age may be attributable to the close temporal relationship between metamorphism and magmatic crystallization, which can greatly influence lead behavior in zircon. Despite this slight variance, the data are statistically sound and we interpret the crystallization age of G8 to be 635.20 ± 5.60 Ma.

4.2.4. G10 (Monzogranite)

Zircons from G10 are very similar to G8, with lengths ranging from 75 to 250 µm and a 4:1 aspect ratio. Color varies from pale yellow, pink, to clear. Grains are often opaque, and all grains are elongated and prismatic pyramidal. A homogenous core surrounded by concentric oscillatory zoning that exhibits recrystallization features, followed by a thick, homogenous rim, almost universally characterizes internal

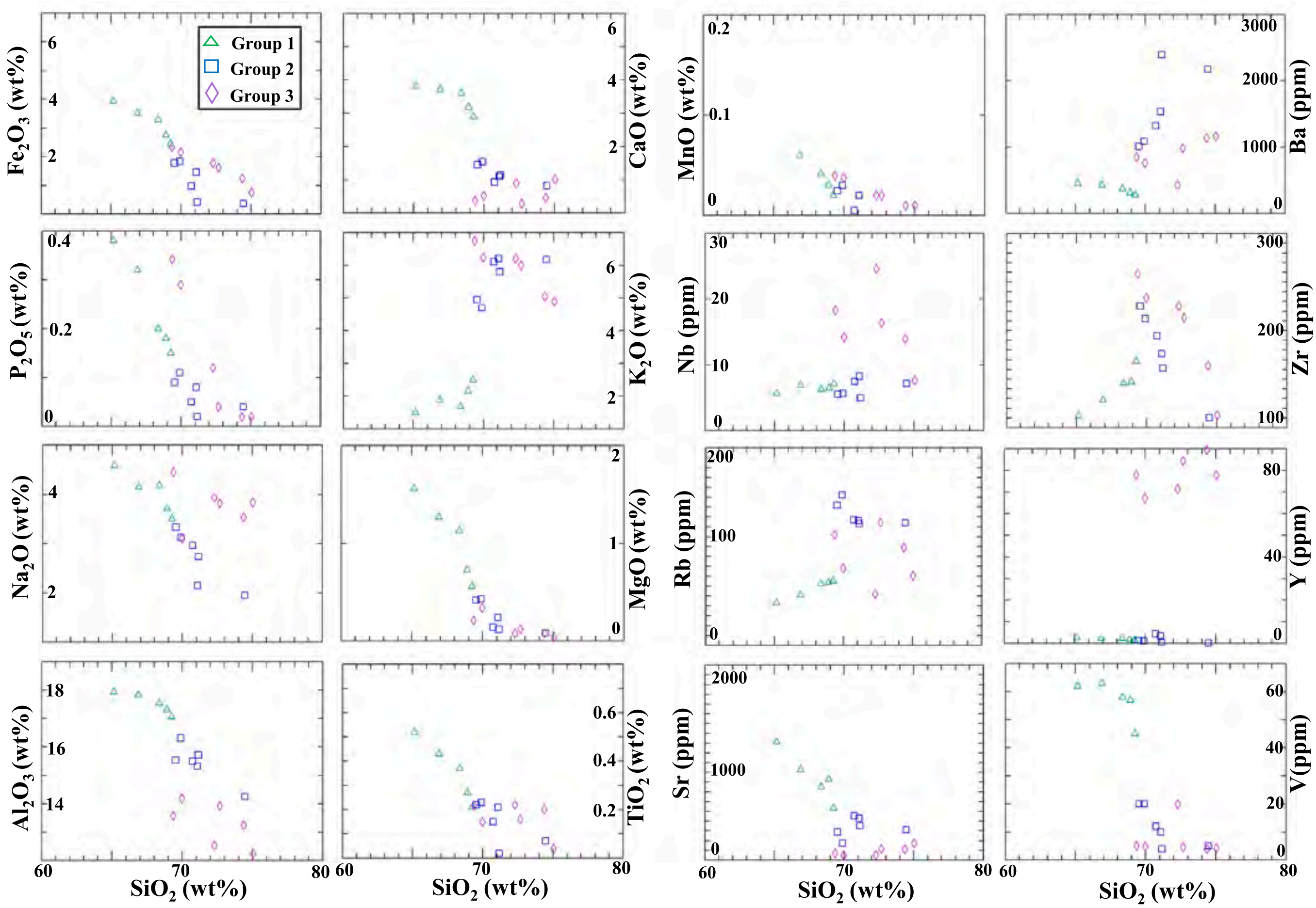

Fig. 6. . Major, minor, and trace element Harker diagrams. Samples are sorted into groupings based on field, petrographic, and geochemical criteria.

zoning.

A total of 30 grains were analyzed of which 29 spots returned concordant scans. Ages range from 683 to 583 Ma and define a single plateau on the weighted mean diagram. Three scans were below a Th/U ratio of 0.1, two of which are some of the youngest ages and all of which were taken on recrystallized rims, suggesting metamorphic recrystallization. Additionally, three scans, although concordant, have very high 2σ (> 45) and are excluded from age calculation. All concordant scans yield a concordia age of 636.20 ± 2.5 Ma (MSWD = 1.3). Without the low Th/U ratio scans and those scans with high error, the concordia age is 638.80 ± 2.70 Ma (MSWD = 0.56) (Fig. 5G) and the $^{206}Pb/^{238}U$ age is 637.70 ± 3.10 Ma (MSWD = 0.97) (Fig. 5H). Considering the lower MSWD, 638.80 ± 2.70 Ma is interpreted as the crystallization age of the G10 rocks.

4.2.5. G16 (Syenogranite)

G16 contains zircons that are pale yellow, clear, and pink, which range from translucent to opaque. The shape is subhedral, subrounded, and rarely rounded. Length varies from 75 to 220 µm, and aspect ratio is generally 2:1. Inclusions are abundant, and zonation tends to be weakly oscillatory, often patchy or planar, and shows clearly recrystallized outer rims.

An age range of 804–686 Ma was calculated from concordant scans on 29 spots. One of the grains was in such close proximity to other grains that the laser spot ablated part of an adjacent grain, and that analysis is therefore left out of age calculations. All Th/U ratios were above 0.1, and the two youngest scans are interpreted as representing Pb loss. Age calculations excluding the two youngest scans and the error scan yield a concordia age of 774.6 ± 2.8 Ma (MSWD = 1.3) (Fig. 5I) and a $^{206}Pb/^{238}U$ age of 773.0 ± 3.10 Ma (MSWD = 1.3) (Fig. 5J). The slight variation does not seem significant when compared with the other data, and we accept the concordia age as the most likely crystallization age.

4.2.6. G18 (Migmatite)

G18 zircons taken from the migmatite's paleosome are comparatively uniform, with length ranging from 100 to 175 µm and an aspect ratio of 2 or 3:1. Zircons are generally clear and have a well-developed euhedral pyramidal shape. Zoning is generally absent except for the outer rims that show very slight overgrowth.

Zircon grain analysis (n = 30) yielded concordant ages between 856 and 631 Ma and a total concordia age of 761.30 ± 3.10 Ma (MSWD = 1.8) (Fig. 5K). The youngest two spots yielded ages 69 Ma and 19 Ma younger than the next youngest grain, and may be the result of Pb loss or later metamorphism. Out of the 30 grains, only four had Th/U ratios > 0.1, which, when considered alongside the lack of clear zoning and petrographic characteristics, point strongly towards a metamorphic origin. Those grains with Th/U > 0.1 may either be anomalies or could represent relict cores from inherited zircons that were originally not formed through metamorphism. Excluding the youngest two analyses due to their large variance from the mean, D18 gives a concordia age of 773.46 ± 3.25 Ma (MSWD = 0.025) (Fig. 5K) and a $^{206}Pb/^{238}U$ age of 775.22 ± 6.47 Ma (MSWD = 3.43) (Fig. 5L). Although the former has a lower MSWD, the latter is older than the crystallization ages of G16, which agrees with the observed field relationships and is therefore considered the original crystallization age of G18. The large spread of ages (856–702 Ma) may be due to a combination of factors such as Pb loss, subsequent metamorphism of the

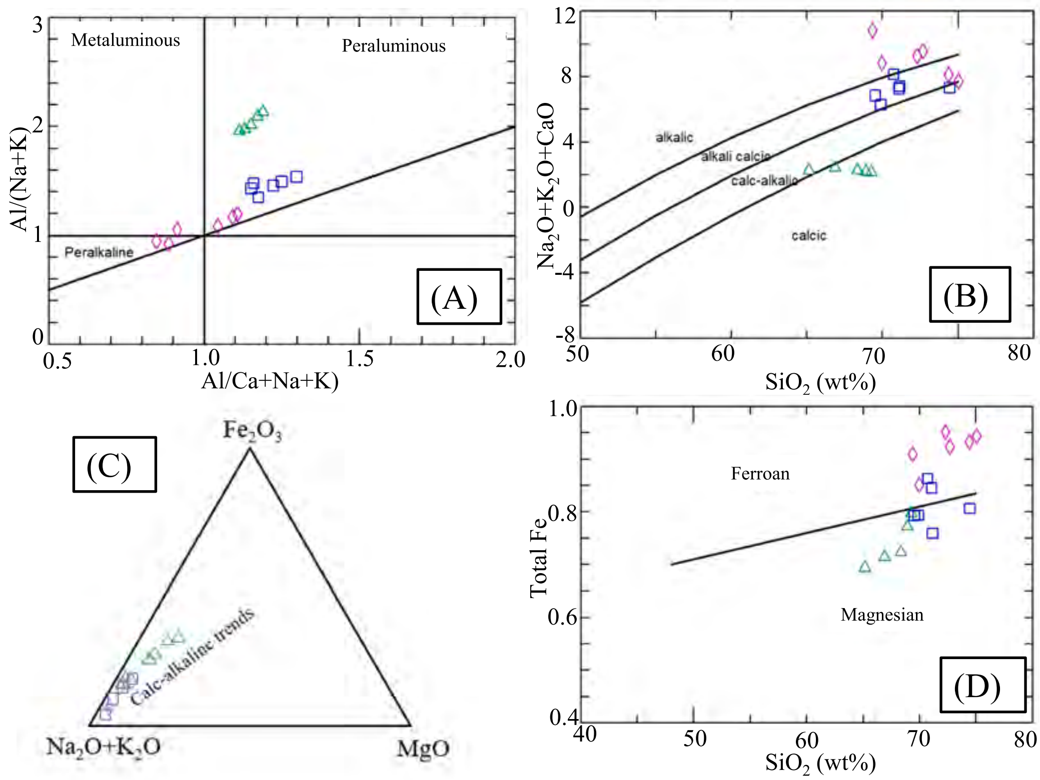

Fig. 7. . Geochemical plots after Maniar and Piccoli (1989), Frost et al. (2001), and Frost and Frost (2008), showing characteristics of the different rock groups. Rock group symbols are shown in Fig. 6.

migmatite, and inherited zircon characteristics. The age and zircon characteristics of the paleosome closely resemble the granodiorites (G1), which may suggest a genetic relationship given their geochemical and spatial similarities.

4.3. Geochemistry

For reference ease and to illustrate genetic relationships among certain rocks, the samples have been classified into three major groups based on similarities in petrography, geochemistry, and U-Pb ages. The granodiorites are a group on their own (Group 1), the second group is composed of the N-S folded monzogranites, and the third group includes the NE-SW folded monzogranites and syenogranites. Since the migmatites represent rocks that have undergone greater chemical alteration than the granites, they are not as useful in tectonic discrimination and thus constitute a grouping of their own.

Overall, both the plutonic rocks and migmatites display a narrow SiO_2 range of 65.14–75.03% and 62.64–69.98%, respectively. Group 1 has the lowest SiO_2 content and higher Al, Fe, Mg, Ca, and Na than the other groups, with Na being particularly high at > 3.4%. Trace element concentrations are high in Sr (535–1210 ppm) and V (45–63 ppm), while low to moderate in Ba (279–453 ppm), Rb (43–65 ppm), and Y (1.33–2.57 ppm). Harker diagrams (Fig. 6) show decreasing Ti, Al, Fe, Mn, Mg, Ca, Na, P, and Sr, while increasing K, Rb, and Zr with increasing Si.

Group 2 has generally low Na (1.95–3.34%), Ca (0.8–1.5%), and Y (0.27–4.4 ppm). On Harker diagrams, Ti, Fe, Mn, Mg, Ca, Na, P, and Zr decrease with increasing Si, while Al, K, and Ba increase. Rb and Sr seem to remain consistent with increasing Si.

Group 3 has low Al (12.25–14.19%), Ca (0.29–1.0%), Mg (0.04–0.34%), Sr (49–174 ppm), and V (4.2–5.12 ppm), while having high contents of many HFS elements such as NB (7.6–24.6 ppm), Y (67–89 ppm), and Zr (113–258 ppm). Group 3 rocks show decreasing Fe, Mn, Mg, Na, K, P, Zr and increasing Y with increasing Si. Like Group 2, Rb and Sr are relatively constant with increasing Si.

According to Shand's Index (Maniar and Piccoli, 1989), Groups 1 and 2 are peraluminous (ASI > 1.11) (Fig. 7A). Group 3 is varied, with samples split among the peraluminous, metaluminous, and peralkaline fields (ASI = 0.84–1.1). The modified alkali lime index (MALI; Frost et al, 2001; Frost and Frost, 2008) vs. SiO_2 puts Group 1 in mostly in the calc-alkalic field,Group 2 in the alkali calcic field, and Group 3 in the alkali and alkali calcic fields (Fig. 7B). All plutonic rock groups plot as calc-alkaline series in an AFM diagram (Fig. 7C). Group 1 and 3 are consistently magnesian and ferroan, respectively, while Group 2 has samples that plot in both fields (Fig. 7D) (Frost and Frost, 2008).

5. Discussion

5.1. Tectonic discrimination

The older rocks (G1–5, G14–20) record all three deformation events (D1–D3), three folding events (F1–F3), and two metamorphic events (M1 and M2) previously described in the WES (Alemu and Abebe, 2000; Ayalew and Johnson, 2002; Johnson et al., 2004; Alemu and Abebe, 2007). D1 deformation and F1 folding are observed only in the older rocks by NE-SW folding, indicating NW-SE-directed compression during early volcanic arc initiation and collision (Fig. 4A). The absence of D1 and F1 deformation and folding in Group 2 rocks supports their younger age interpretation.

D2 and D3 deformation, F2 and F3 folding, and F3-related shearing are observed in all rocks within the study area and is recorded by asymmetrical folding that strikes N-S (F2), suggesting a stress rotation during Mozambique Ocean closure. D3 and F3 are evidenced in thin section as shear bands and augens, as well as outcrop-scale dextral shear structures. These features from the D3 deformation event are associated with a late crustal thickening stage (post 650 Ma), and

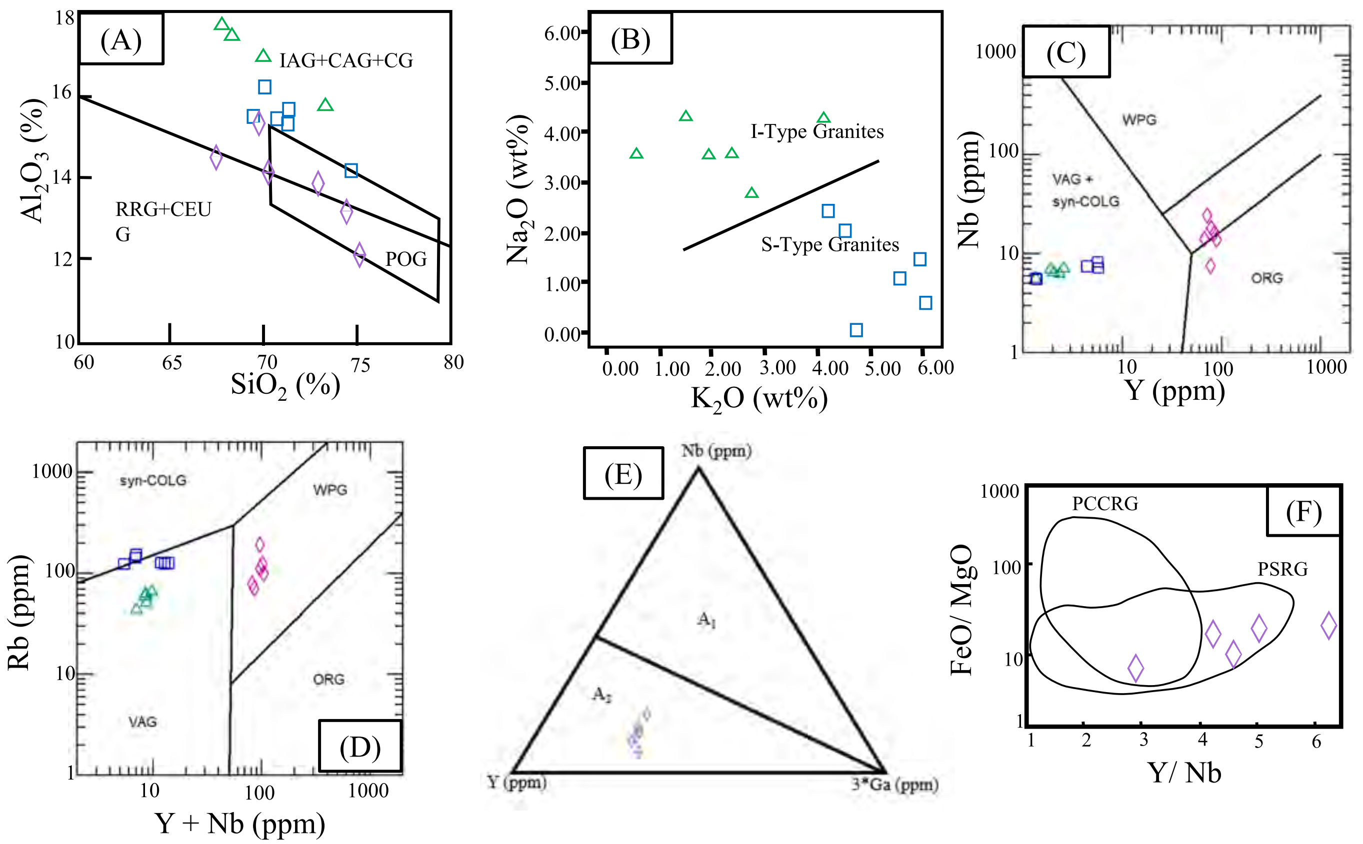

Fig. 8. . (A–D) Tectonic discrimination diagrams of the different granite groups from Pearce et al. (1984) and Whalen et al. (1987). Group 1 rocks plot as volcanic arc granites (VAG), island arc granites (IAG), continental arc granites (CAG), collisional granites (CG), and I-type granites. Group 2 plots as IAG, CAG, CG, S-type, and, variably, VAG and syn collisional (*syn*-COLG) granites. Group 3 tends to be within plate granites (WPG) and post-collisional granites (POG), although a slight spread exists. (E & F) Discrimination diagrams from Maniar and Piccoli (1989) and El Dabe (2013) further clarify the Group 3 granites into A2 (continental collision or island arc magmatism) and post subduction related granites (PSRG). Rock group symbols are shown in Fig. 6.

indicate that the rocks underwent deformation at depth that post-dates granite crystallization in the study area (Ayalew and Johnson, 2002; Alemu and Abebe, 2007).

Tectonic discrimination diagrams plot the granodiorites as volcanic arc granites (VAG) (Fig. 8A–D). Low Nb, low Rb/Sr ratio (< 0.2), high Sr, and increasing molar A/CNK (Al_20_3 / (CaO + Na_2O + K_2O) with increasing Si supports an origin in a subduction-related environment. Furthermore, multi-element diagrams show large ion lithophile element (LILE) enrichment and high field strength elements (HFSE) depletion, which is characteristic of arc magmatism (Gill, 1981). These rocks are the oldest rocks within the study area with a U-Pb age of 797.60 ± 4.80 Ma, indicating that the oldest intrusion in this area formed from arc magmatism.

Group 2 rocks plot at the boundary of the VAG and syncollisional granite (*syn*-COLG) (Fig. 8C and D). The Na vs. K plot suggests that the Group 2 rocks may be anatectic in origin (Fig. 8B). The presence of muscovite, ilmenite, garnet, and cordierite, the lack of magnetite, and the presence of inherited zircons in these rocks supports a crustal origin, classifying these rocks as S-type (Chappell and White, 1974). Crustal signals are also observed in the moderate to high Rb/Sr (characteristics of crustal melt), Th/La (characteristics of crustal contamination), and K/Na, the latter of which may be due to K being incorporated into the clay while Na is removed during weathering. Furthermore, geochemical characteristics such as low Na ($< 3.2\%$), Ca, Y, and steady A/CNK with increasing Si are characteristic of S-type granites (Chappell and White, 1974). The younger age (635–638 Ma) and geochemical trends of these granites suggest that their formation may be related to country rock anatexis during crustal thickening around the time of the D3 deformational event.

Group 3 rocks consistently plot as within plate (WPG) and A-type granites, and can be further classified into A2, postorogenic (POG), and post subduction related (PSRG) granites, all of which suggest a formation linked to subduction (Fig. 8A–F). Geochemical characteristics such as high amounts of incompatible elements, high K/Na, Fe/Mg, Ti/Mg, Ga/Al, Fe/Fe + Mg, HFS, as well as low Al, Ca, Mg, Sr, and V agree with an interpretation as a post-subduction related granite (Pearce et al., 1984; Whalen et al., 1987; Eby, 1990, 1992). Additionally, A-type granites have been long identified as being “dry,” from melting of an anhydrous source, and lack of hydrous minerals such as chlorite and sericite and presence of interstitial biotite and amphibole point to anhydrous melting in this rocks (Collins et al., 1982).

5.2. Geochemical evolution and petrogenesis

All rocks from the study area exhibit some degree of metamorphism, and the metamorphic events that affected the rocks may have led to chemical metamorphic alterations. However, smooth trends in the major, minor, and trace element plots and no significant correlation between incompatible and compatible trace elements suggest that the rocks have largely preserved their original magmatic signatures and characteristics. Hence, geochemical investigation of the rocks may give insight to the magmatic conditions in which these rocks formed and the parental material from which they crystallized.

Geochemical and mineralogical characteristics of the Group 1 rocks such as high Na ($> 3.2\%$) a positive correlation between A/CNK and Si, and the presence of amphibole and magnetite classify the Group 1 rocks as I-type granites (Chappell and White, 1974). Likewise, the low (< 60) Al/Ti ratio of the Group 1 rocks may indicate an origin from the high

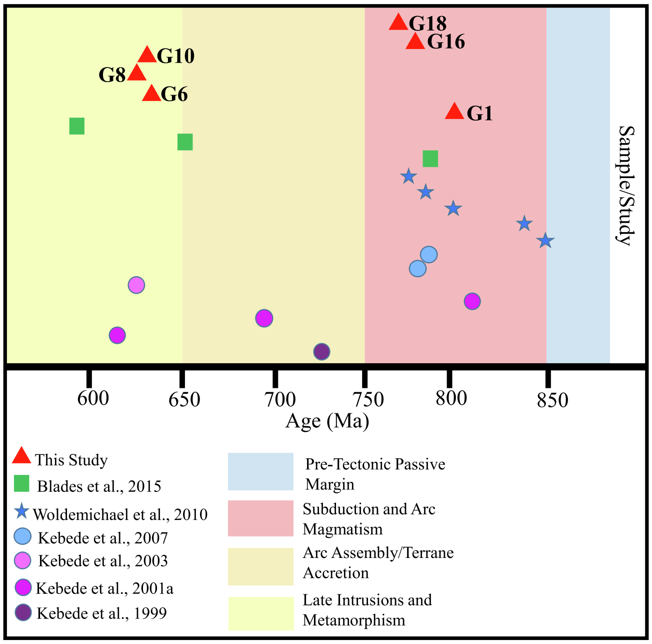

Fig. 9. . Comparison of granite and gneiss ages across the WES in correlation with tectonic events. The granodiorite (G1), syenogranite (G16), and migmatite (G18) fall within an early magmatic period characterized by subduction initiation and metamorphism. The monzogranites (G8, G6, G10) represent a later magmatic episode that likely produced melt through anatexis during continental collision. Vertical axes represent an arrangement of different samples within each study.

temperature melting of basaltic underplating. Such a geochemical makeup closely resembles adakitic characteristics, which supports formation from mafic underplating during subduction. Petrographic characteristics such as the presence of sericite and chlorite suggest that hydrous melting was involved in the rock's formation.

Group 2 rocks display chemical characteristics of both subduction and anatectic-related melts. All of these rocks have low Nb, which is associated with subduction-related melts, but high Ba, and Rb, which points towards crustal contamination. These rocks are also rich in aluminous minerals such as biotite and muscovite, which is generally indicative of anatectic granites. These rocks might therefore be cautiously classified as S-type granites, indicating an anatectic component.

Several modes of A-type granite formation have been identified in literature, such as basalt fractionation, partial melting of a tonalitic source, and melting of a dehydrated residual source (McCarthy and Hasty, 1976; Loiselle and Wones, 1979; Cullers et al., 1981; Collins et al., 1982; Creaser et al., 1991; Turner et al., 1992; Skjerlie and Johnston, 1993). Due to their geochemical characteristics, we do not consider the first two formational modes viable options for the Group 3 rocks. The third method of melting a residual source requires I-type production to dehydrate and deplete the source, increasing disorder in the melt and allowing HFS elements to be incorporated into the elemental framework (Collins et al., 1982). Given the similar geochemical characteristics, we consider it possible that our Group 3 rocks were produced from a residual source that was dehydrated, but not geochemically depleted, from the formation of Group 1 or similar I-type magmas. A similar situation was expounded upon in Landenberger and Collins (1996), who showed that partial melting of an I-type magma depleted only parts of the source rock while dehydrating larger areas. This effectively charnockitized the lower crust, leaving alkali feldspar as a stable phase. The lower crust was then heated during continued underplating, raising temperatures to melt the anhydrous source. Without isotope data, the anhydrous and alkali feldspar rich nature of the A-types, along with their relationships to the I-types, suggests formation from a dehydrated, but not geochemically depleted, lower crustal source during the final stages of subduction.

5.3. Regional tectonic correlation

Other arc-related granitoids have been reported throughout the WES by various studies (e.g. Wolde, 1996; Ayalew and Peccerillo, 1998; Kebede et al., 1999, 2001a; Woldemichale et al., 2010; Blades et al., 2015), with ages ranging from 729 to 815 Ma (Fig. 9). Woldemichale et al. (2010) reported an island arc-related diorite 60 km to the northwest of ages 787.7 ± 8.8 Ma and 794.3 ± 9.4 Ma, which is synchronous with sample D1. These rocks represent an early stage of magmatism associated with the East African Orogen and the initial closing of the Mozambique Ocean (Fig. 10A and B).

Given the similar geochemical and geochronological characteristics between the Group 1 rocks and the migmatites (Group 4), Group 4 rocks may represent migmatized granites genetically related to Group 1 rocks. Blades et al. (2015) presented a quartzo-feldspathic gneiss 6 km to the south of our study area that formed 782 ± 33 Ma, which is within the range of our migmatite's 775.22 ± 3.43 Ma U-Pb age (Fig. 9). Therefore, metamorphism around 780–760 Ma may have formed the migmatitic texture in the Group 4 rocks shortly after the magmatic episode during which Group 1 and 4 rocks were emplaced (Ayalew et al., 1990; Ayalew and Peccerillo, 1998).

While other A-type granites in the WES date to late or post tectonic crystallization, geochronological studies are severely lacking (e.g. Kebede et al., 1999, 2001b; Kebede and Koeberl, 2003). Consequently, our rocks represent the oldest dated A-type granite magmatism in the WES. The significance of our A-type granites is that they signal the final stages of subduction in this part of the WES (Fig. 10C).

The age of Group 2 rocks (635–638 Ma) aligns with a previously reported 635–580 Ma magmatic episode in the WES, suggesting that crustal thickening associated with micro-continental collision may be the melting mechanism that formed these rocks (Fig. 10D; Ayalew and Peccerillo, 1998; Ayalew and Johnson, 2002; Johnson et al., 2004). Ayalew and Peccerillo (1998), Kebede et al. (2001a, 2001b), Greene et al. (2003), and Blades et al. (2015) also reported anatectic granites from the WES, dating to a wide age range between ~ 700 and 540 Ma. The nearby Suqqii-Wagga granite also formed from crustal thickening (Kebede et al., 2001a, 2001b), and Ayalew and Peccerillo (1998) identified anatectic granite formation from partial melting of calc-alkaline intrusives, geochemically similar to this study's anatectic granites. An anatectic granite studied by Blades et al. (2015) 6–8 km south of our study area is dated to 653 ± 12 Ma, which is in close alignment with this study's granite ages (Fig. 9). Given their age, the Group 2 granites formed during the last stage of the WES's main deformational period.

6. Conclusions

U-Pb crystallization ages, structural characteristics, and geochemical trends of the Dabana granites present a protracted collisional history related to the East African Orogen and closure of the Mozambique Ocean. The formational history of these rocks is summarized as follows:

1) Subduction-related magmatism caused mafic underplating that formed an I-type adakitic granodiorite dating to 797.6 Ma. Production of this I-type granite dehydrated much of the source region, yet left some areas geochemically enriched.
2) High-grade metamorphism during collision formed migmatite at 775.22 Ma, which may have a genetic relationship to the previous I-type granite emplacement.
3) Post-subduction related magmatism in the same area signaled the final subduction stages and beginning of micro-continent collision. Continued underplating supplied necessary heat to melt the now dehydrated, yet still geochemically enriched source rocks. Evidence

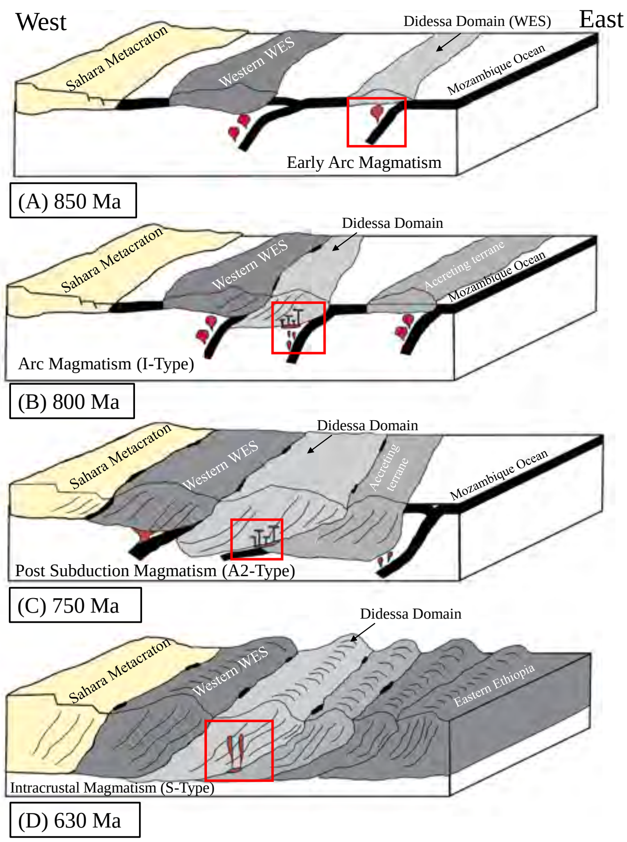

Fig. 10. . Tectonic models modified from Ayalew and Johnson (2002), Greene et al. (2003), and Blades et al. (2015, 2017) to include this study's conclusions based on geochronologic ages, trace element tectonic discriminations, and elemental trends. (A) The beginning stages of the Mozambique Ocean closure initiated subduction zones and volcanic arcs. (B) Continued closure of the Mozambique Ocean led to magmatic arc formation during subduction-related magmatism. The Group 1 rocks formed during this stage from a hydrous source at 797 Ma. (C) Towards the final subduction stages, magmatism from a dehydrated source created the material for the Group 3 rocks. (D) Late-stage crustal thickening initiated melting that created the Group 2 rocks with a crustal signature (modified after Ayalew and Johnson, 2002; Blades et al., 2015, 2017).

for post-subduction magmatism is recorded in A2-type granites that date to 774.6 Ma.

4) Late-stage crustal thickening between 639 and 635 Ma formed granite with crustal geochemical signals, which was then followed by subsequent metamorphism.

Funding

This work was supported by the American Chemical Society Petroleum Research Fund [#PRF 54500-UNI8], the Geological Society of America Graduate Student Research Grant, the Western Kentucky University (WKU) Lifetime Experience Grant, and WKU Graduate Student Research Grant.

Declaration of Competing Interest

The authors declare that they have no known competing financial interests or personal relationships that could have appeared to influence the work reported in this paper.

Acknowledgements

Acknowledgment is made to the donors of the American Chemical Society Petroleum Research Fund (#PRF 54500-UNI8) to Gani for support of this research. Partial support of this research came from the Western Kentucky University (WKU) Lifetime Experience Grant, WKU Graduate Student Research Grant and the Geological Society of America Graduate Student Research Grant to Bowden. We thank Pauline Norris at WKU Advanced Materials Institute, John Andersland at WKU Electron Microscopy (EM) Laboratory, and Jason Backus at the Kentucky Geological Survey for their lab assistance. We would like to thank Ayele Sode who was invaluable with his assistance in sample shipping. We would also like to thank Abigail Bowden for assisting in the field. Special thanks goes out to Jim McMillan, Victoria Cross, and Charlie Taylor of GeoSeps Services for their collaboration and help. Also of great assistance was Dr. Andrew Barth at Indiana University – Purdue University Indianapolis. Finally, we thank the reviewers and editor of Precambrian Research for their indispensible assistance during the review process.

References

Abbate, E., Bruni, P., Sagri, M., 2015,. Geology of Ethiopia: a review and geomorphological perspectives. Landscapes and Landforms of Ethiopia. World Geomorphol. Landscapes 3 (389), 33–64.
Abdelsalam, M., Gao, S., Liegeois, J.-P., 2011. Upper mantle structure of the Saharan Metacraton. J. Afr. Earth Sci. 60, 328–336.
Abdelsalam, M., Stern, R., 1996. Sutures and shear zones in the Arabian-Nubian Shield. J. Afr. Earth Sc. 23 (3), 289–310.
Abdelsalam, M., Tsige, L., Yihunie, T., Hussien, B., 2008. Terrane rotation during the East African Orogeny: evidence from the Bulbul Shear Zone, south Ethiopia. Gondwana Res. 14 (3), 497–508.
Alemu, T., Abebe, T., 2000. Geology of the Gimbi Area. Geological Survey of Ethiopia, Memoir 15, 158.
Alemu, T., Abebe, T., 2007. Geology and tectonic evolution of the pan-African Tulu Dimtu Belt, Western Ethiopia. Online J. Earth Sc. 1 (1), 24–42.
Alemu, T., 2014 (compiler). Geological Map of the Arjo Area. Geological Survey of Ethiopia, Memoir 23, 83.
Allen, A., Tadesse, G., 2003. Geological setting and tectonic subdivision of the Neoproterozoic orogenic belt of Tuludimtu, western Ethiopia. J. Afr. Earth Sc. 36, 329–343.
Avigad, D., Stern, R., Beyth, M., Miller, N., McWilliams, M., 2007. Detrital zircon U-Pb geochronology of Cyrogenian diamictites and Lower Paleozoic sandstone in Ethiopia (Tigrai): age constraints on Neoproterozoic glaciation and crustal evolution of the southern Arabian-Nubian Shield. Precambr. Res. 154, 88–106.
Ayalew, T., Bell, K., Moore, J., Parrish, R., 1990. U-Pb and Rb-Sr geochronology of the Western Ethiopian Shield. Geol. Soc. Am. Bull. 102, 1309–1316.
Ayalew, T., Peccerillo, A., 1998. Petrology and geochemistry of the Gore-Gambella plutonic rocks: implications for magma genesis and the tectonic setting of the Pan-African Orogenic Belt of western Ethiopia. J. Afr. Earth Sc. 27 (3–4), 397–416.
Ayalew, T., Johnson, T., 2002. The geotectonic evolution of the Western Ethiopian Shield. Ethiopian J. Sc. 25 (2), 227–252.
Bingen, B., Viola, J., Henderson, I., Skar, O., Boyd, R., Thomas, R., Solli, A., Key, R., Daudi, E., 2009. Geochronology of the Precambrian crust in the Mozambique belt in NE Mozambique and implications for Gondwana assembly. Precambr. Res. 170, 231–255.
Blades, M., Collins, A., Foden, J., Payne, J., Xu, X., Alemu, T., Woldetinsae, G., Clark, C., Taylor, R., 2015. Age and hafnium isotopic evolution of the Didessa and Kemashi Domains, western Ethiopia. Precambr. Res. 270, 267–284.
Blades, M., Foden, J., Collins, A., Alemu, T., Woldetinsae, G., 2017. The origin of the ultramafic rocks of the Tulu Dimtu Belt, western Ethiopia – do they represent remnants of the Mozambique Ocean? Geol. Mag. 1–21.
Bonavia, F., Chorowicz, J., 1992. Northward expulsion of the Pan-African of northeast Africa guided by a reentrant zone of the Tanzania craton. Geology 20, 1023–1026.
Chappell, B.W., White, A.J.R., 1974. Two contrasting granite types. Pac. Geol. 8, 173–174.
Chen, T., 2001. The Mozambique Belt: the link between East and west Gondwana in the Neoproterozoic and possible connection with the Trans-Antarctic Mountains. Gondwana Res. 4, 594–595.
Collins, W.J., Beams, S.D., White, A.J.R., Chappell, B.W., 1982. Nature and origin of A-type granites with particular reference to southeastern Australia. Contrib. Mineralol. Petrol. 80, 189–200.
Creaser, R.A., Price, T.C., Wormold, R.J., 1991. A-type granites revisited: assessment of a residual-source model. Geology 19, 163–166.
Cullers, R.J., Kock, R.J., Bickford, M.E., 1981. Chemical evolution of magmas in the Proterozoic terrane of the St. Francois Mountains, southeastern Missouri. J. Geophys. Res. B86, 10388–110301.
De Waele, B., Kampunzu, A., Mapani, B., Tembo, F., 2006. The Mesoproterozoic Irumide belt of Zambia. J. Afr. Earth Sc. 46, 36–70.
Divi, R., Zakir, F., Al-Mishwat, A., 2001. Structure and Metallogenic framework of the Arabian Shield, the northern join between East and West Gondwana. Gondwana Res. 4, 607–608.
Eby, G., 1990. The a-type granitoids: a review of their occurrence and chemical characteristics and speculations on their petrogenesis. Lithos 26, 115–134.

Eby, G., 1992. Chemical subdivision of the A-type granitoids: petrogenetic and tectonic implications. Geology 20, 641–644.

El Dabe, M., 2013. A geochemical tectonomagmatic classification of the A-type granitoids based on their magma types and tectonic regimes. Arabian J. Geosci. 8 (10), 187–193.

Fritz, H., Abdelsalam, M., Ali, K., Bingen, B., Collins, A., Fowler, A., Ghebreab, W., Hauzenberger, C., Johnson, P., Kusky, T., Macey, P., Muhongo, S., Stern, R., Viola, G., 2013. Orogen styles in the East African Orogen: a review of the Neoproterozoic to Cambrian tectonic evolution. J. Afr. Earth Sc. 86, 65–106.

Frost, B., Barnes, C., Collins, W., Arculus, R., Ellis, D., Frost, C., 2001. A geochemical classification for granitic rocks. J. Petrol. 42 (11), 2033–2048.

Frost, B., Frost, C., 2008. A geochemical classification for feldspathic igneous rocks. J. Petrol. 49, 1955–1969.

Gerra, S., Hailemariam, M., 2000. Geology of The Nekemte Area. Geological Survey of Ethiopia, Memoir 14, 110.

Gill, J., 1981. Orogenic Andesites and Plate Tectonics. Minerals and Rocks, Springer-Verlag, Berlin 16.

Goodenough, K., Thomas, R., De Waele, B., Key, R., Schofield, D., Bauer, W., Tucker, R., Rafahatelo, J., Rabarimanana, M., Ralison, A., Randriamananjara, T., 2010. Post-collisional magmatism in the central East African Orogen: the Maevarano Suite of north Madagascar. Lithos 116 (1–2), 18–34.

Greene, T., Pedersen, R., Bjerkgard, T., Braathen, A., Selassie, M., Worku, T., 2003. Neoproterozoic evolution of Western Ethiopia: igneous geochemistry, isotope systematics and U-Pb ages. Geol. Mag. 140 (4), 373–395.

Johnson, T., Ayalew, T., Mogessie, A., Kruger, F., Poujol, M., 2004. Constraints on the tectonometamorphic evolution of the Western Ethiopian Shield. Precambr. Res. 133, 305–327.

Johnson, P., Andresen, A., Collins, A., Fowler, A., Fritz, H., Ghebreab, W., Kusky, T., Stern, R., 2011. Late Cryogenian-Ediacaran history of the Arabian-Nubian Shield: a review of depositional, plutonic, structural, and tectonic events in the closing stages of the northern East African Orogen. J. Afr. Earth Sc. 61, 167–232.

Kebede, T., Koeberl, C., Koller, F., 1999. Geology, geochemistry and petrogenesis of intrusive rocks of the Wallagga area, western Ethiopia. J. Afr. Earth Sc. 29 (4), 715–734.

Kebede, T., Koeberl, C., Koller, F., 2001a. Geology, geochemistry and petrogenesis of intrusive rocks of the Wallaga area, western Ethiopia. J. Afr. Earth Sc. 29 (4), 715–734.

Kebede, T., Kloetzli, U., Koeberl, C., 2001b. U/Pb and Pb/Pb zircon ages from granitoid rocks of Wallagga area: constraints on magmatic and tectonic evolution of Precambrian rocks of western Ethiopia. Mineral. Petrol. 71, 251–271.

Kebede, T., Koeberl, C., 2003. Petrogenesis of A-type granitoids from the Wallagga area, western Ethiopia: constraints from mineralogy, bulk-rock chemistry, Nd and Sr isotopic compositions. Precambr. Res. 121, 1–24.

Kebede, T., Horie, K., Hidaka, H., Terada, K., 2007. Zircon 'microvein' in peralkaline granitic gneiss, western Ethiopia: Origin, SHRIMP U-Pb geochronology and trace element investigations. Chem. Geol. 242, 76–102.

Landenberger, B., Collins, W., 1996. Derivation of A-type granties from a dehydrated charnockitic lower crust: evidence from the Chaelundi Complex, eastern Australia. J. Petrol. 37 (1), 145–170.

Loiselle, M.C., Wones, D.R., 1979. Characteristics and Origin of Anorogenic Granites. Geological Society of America, Abstracts with Programs 11, 468.

Maniar, P., Piccoli, P., 1989. Tectonic discrimination of granitoids. Geol. Soc. Am. Bull. 101, 635–643.

Meert, J., Lieberman, B., 2008. The Neoproterozoic assembly of Gondwana and its relationship to the Ediacaran-Cambrian radiation. Gondwana Res. 14 (102), 5–21.

McCarthy, T., Hasty, R., 1976. Trace element distribution patterns and their relationship to the crystallization of granitic melts. Geochem. Cosmochim. Acta 40 (11), 1351–1358.

Moller, A., Mezger, K., Schenk, V., 1998. Crustal age domains and the evolution of the continental crust in the Mozambique Belt of Tanzania: combined Sm-Nd, Rb-Sr, and Pb-Pb isotopic evidence. J. Petrol. 39 (4), 749–783.

Muhongo, S., Lenior, J., 1994. Pan African granulite facies metamorphism in the Mozambique Belt of Tanzania: U-Pb zircon geochronology. J. Geol. Soc. 151, 343–347.

Muhongo, S., Kroner, A., Wallbrecher, E., Sommer, H., 2001. Cross-section through the Mozambique Belt of East Africa and implications for Gondwana assembly. Gondwana Res. 4 (4), 709–710.

Pearce, J., Harris, N., Tindle, A., 1984. Trace element discrimination diagrams for the tectonic interpretation of granitic rocks. J. Petrol. 25, 956–983.

Skjerlie, K.P., Johnston, A.D., 1993. Fluid-absent melting behavior of a F-rich tonalitic gneiss at mid-crustal pressures: implications for the generation of anorogenic granites. J. Petrol. 34, 785–815.

Stacey, J., Kramer, J., 1975. Approximation of terrestrial lead isotope evolution by a two-stage model. Earth Planet. Sci. Lett. 26 (2), 207–221.

Stern, R., Kroner, A., 1993. Late Precambrian crustal evolution in the NE Sudan: isotopic and geochronological constraints. J. Geol. 101, 555–574.

Stern, R., 1994. Arc assembly and continental collision in the Neoproterozoic East African Orogen: Implications for the consolidation of Gondwanaland. Ann. Rev. Earth Planetary Sc. 22, 319–351.

Stern, R., 2002. Crustal evolution in the East African Orogen: a neodymium isotopic perspective. J. Afr. Earth Sc. 34 (3–4), 109–117.

Stern, R., Ali, K., Liegeois, J., Johnson, P., Kozdroj, W., Kattan, F., 2010. Distribution and significance of pre-Neoproterozoic zircons in juvenile Neoproterozoic igneous rocks of the Arabian-Nubian shield. Am. J. Sci. 310, 791–811.

Stern, R., Ali, K., Abdelsalam, M., Wilde, S., Zhou, Q., 2012. U-Pb zircon geochronology of the eastern part of the Southern Ethiopian Shield. Precambr. Res. 206–207, 159–167.

Tefera, M., Berhe, S., 1987 (compliers). Geological Map of Gore. Ethiopian Institute of Geological Surveys, Ministry of Mines and Energy.

Teklay, M., Kroner, A., Mezger, K., Oberhansli, R., 1998. Geochemistry, Pb-Pb single zircon ages and Nd-Sr isotope composition of Precambrian rocks from southern and eastern Ethiopia: implications for crustal evolution in East Africa. J. Afr. Earth Sc. 26 (2), 207–227.

Tsige, L., Abdelsalam, M., 2005. Neoproterzoic – early Paleozoic gravitational tectonic collapse in the southern part of the Arabian-Nubian Shield: the Bulbul Belt of southern Ethiopia. Precambr. Res. 138, 297–318.

Tsige, L., 2006. Metamorphism and gold mineralization of the Kenticha-Katawicha area: Adola belt, southern Ethiopia. J. Afr. Earth Sc. 45, 16–32.

Turner, S.P., Foden, J.D., Morrison, R.S., 1992. Derivation of some A-type magmas by fractionation of basaltic magma: an example from the Padthaway Ridge, South Australia. Lithos 28, 151–179.

Vermeesch, P., 2018. IsoplotR: a free and open toolbox for geochronology. Geosci. Front.

Whalen, J., Currie, K., Chappell, B., 1987. A-type granites: geochemical characteristics, discrimination and petrogenesis. Contrib. Miner. Petrol. 95, 407–419.

Wolde, B., Gore-Gambella Geotraverse Team, 1996. Tonalite-trondhjemite-granite genesis by partial melting of newly underplated basaltic crust: an example from the Neoproterozoic Birbir magmatic arc, western Ethiopia. Precambr. Res. 70, 3–14.

Woldemichale, B., Kimura, J., Dunkley, D., Tani, K., Ohira, H., 2010. SHRIMP U-Pb zircon geochronology and Sr-Nd isotopic systematic of the Neoproterozoic Ghimbi-Nedjo mafic to intermediate intrustions of Western Ethiopia: a record of passive margin magmatism at 855 Ma? Int. J. Earth Sc. 99, 1773–1790.

Worku, H., 1996. Geodynamic development of the Adola Belt (Southern Ethiopia) in the Neoproterozoic and its control on gold mineralization. (Doctoral thesis). Technische Universität Berlin.

Worku, H., Schandelmeier, H., 1996. Tectonic evolution of the Neoproterozoic Adola Belt of Southern Ethiopia: evidence for a Wilson Cycle process and implications for oblique plate collision. Precambr. Res. 77, 179–210.

Yibas, B., Reimold, W., Armstrong, R., Koeberl, C., Anhaeusser, C., Phillips, D., 2002. The tectonostratigraphy, granitoid geochronology and geological evolution of the Precambrian of southern Ethiopia. J. Afr. Earth Sc. 34, 57–84.

Yihunie, T., Tesfaye, M., 2002. Structural evidence for the allochthonous nature of the Bulbul terrane in southern Ethiopia: a west-verging thrust nappe. J. Afr. Earth Sc. 34, 85–93.

Yihunie, T., 2003. Chemical Th-U-total Pb isochron ages of zircon and monazite from granitic rocks of the Negele area, southern Ethiopia. J. Earth Planetary Sc. 50, 1–12.

Yihunie, T., Hailu, F., 2007. Possible eastward tectonic transport and northward gravitational tectonic collapse in the Arabian-Nubian shield of western Ethiopia. J. Afr. Earth Sc. 49 (1), 1–11.